

Generating heat with metal nanoparticles

We describe recent studies on photothermal effects using colloidal nanoparticles. Metal nanoparticles efficiently generate heat in the presence of electromagnetic radiation. This process becomes strongly enhanced under plasmon resonance and also depends on the shape and organization of the nanoparticles. In particular, the amount of generated heat and temperature increase depends on the number of nanoparticles in a complex. Metal nanoparticles may induce phase transformations when they are in thermal contact with a polymer or a solid matrix, such as ice. This suggests new possibilities for measuring heat release at the nanoscale.

Alexander O. Govorov* and Hugh H. Richardson†

Department of Physics and Astronomy, and Department of Chemistry and Biochemistry, Ohio University, Athens, OH 45701, USA
E-mail: *govorov@ohiou.edu; †richards@helios.phy.ohiou.edu

The optical properties of nanoparticles (NPs), including both semiconductor^{1,2} and metal³⁻¹² nanocrystals, have been studied intensively. Recently, another related physical property – heat generation by NPs under optical illumination – has also attracted much interest^{6,13-24}. The heat generation process involves not only absorption of incident photons, but also heat transfer from the NP to the surrounding matrix.

The heating effect is especially strong for metal NPs since they have many mobile electrons. It becomes strongly enhanced under plasmon resonance or when the laser frequency hits the collective resonance of an NP. Since metal NPs have a very low optical quantum yield (i.e. they are very poor light emitters), the total amount of heat generated can be estimated in a relatively simple way as the total optical absorption rate. At the same time, it is more challenging to measure the temperature increase at the surface of the NPs. The temperature

increase is the most important parameter for current applications of heated NPs in nanomedicine²⁵⁻²⁸. An attempt to measure the temperature on the surface of Au NPs directly has recently been performed⁶. It was achieved by embedding Au NPs in ice and driving them optically. Then, by observing the power threshold for the melting process, one can determine the NP surface temperature. Another interesting approach involved assembling a complex made of both semiconductor and metal NPs²⁹. These NPs were linked to each other with a polymer, where the length of the polymer chain changes rapidly with temperature. Since the semiconductor NP emission strongly depends on the distance from the metal nanocrystal, by measuring the emission intensity, one can determine the local temperature within the NP complex.

Biomedical applications of heated NPs rely on a simple mechanism^{25,26}. First, NPs become attached to tumor cells using

selective biomolecular linkers. Then heat generated by optically-stimulated NPs destroys the tumor cells. The important parameter in this process is the temperature at the surface of the NPs and also the collective response of NPs. It is essential that Au NPs are suitable for simultaneous molecular imaging and photothermal cancer therapy^{25,26}. Molecular imaging is based on the strong light scattering of Au NPs. Because of these applications, fundamental studies of photothermal effects become pertinent.

Plasmon resonances in nanocrystals can be tailored. Au nanorods²⁵ and nanoshells³⁰ have plasmon resonances shifted to the red (650-900 nm). This is important to reduce absorption by the biological medium. Heated NPs are also used in photothermal imaging and turn out to be very effective³¹. Heating creates changes in the optical properties (e.g. refractive index) of the inhomogeneous medium and these changes can be recorded optically. Another type of experiment involves phase transformations of the surrounding material under heating. Skirtach *et al.*³² describes remote release of materials (drugs) from a polymer capsule containing Au NPs excited with intense light. This capsule is destroyed as a result of the heating effect, and the researchers observed the melting of the Au-NP-polymer-CdTe-complexes. A similar approach has been used to release the contents of small containers inside living cells³³. Vaporization of water and opto-fluidic effects coming from heated metal NPs have been reported³⁴. Theoretical work³⁵ has described the mechanisms of melting of polymer and ice matrices with embedded Au NPs and the collective thermo-optical responses of metal NPs.

Theoretical background

Heating effects

Crystalline NPs composed of various materials (such as Au, Ag, and semiconductors) can efficiently release heat under optical excitation. The mechanism of heat release is very simple – the laser electric field strongly drives mobile carriers inside the nanocrystals, and the energy gained by carriers turns into heat. Then the heat diffuses away from the nanocrystal and leads to an elevated temperature of the surrounding medium. Heat generation becomes especially strong in the case of metal NPs in the regime of *plasmon resonance*. Plasmon resonance is a collective motion of a large number of electrons. In the case of semiconductor NPs, the heat generation rate is much weaker since heat dissipation occurs through an interband absorption process with the creation of a single mobile electron and hole (exciton).

In the absence of phase transformations, temperature distribution around optically-stimulated NPs is described by the usual heat transfer equation:

$$\rho(\mathbf{r}) c(\mathbf{r}) \frac{\partial T(\mathbf{r}, t)}{\partial t} = \nabla k(\mathbf{r}) \nabla T(\mathbf{r}, t) + Q(\mathbf{r}, t) \quad (1)$$

where \mathbf{r} and t are the coordinate and time, $T(\mathbf{r}, t)$ is the local temperature, and the material parameters $\rho(\mathbf{r})$, $c(\mathbf{r})$, and $k(\mathbf{r})$ are the

mass density, specific heat, and thermal conductivity, respectively. The function $Q(\mathbf{r}, t)$ represents an energy source coming from light dissipation in NPs:

$$Q(\mathbf{r}, t) = \langle \mathbf{j}(\mathbf{r}, t) \cdot \mathbf{E}(\mathbf{r}, t) \rangle_t \quad (2)$$

where $\mathbf{j}(\mathbf{r}, t)$ is the current density and $\mathbf{E}(\mathbf{r}, t)$ is the stimulating electric field in the system. This field should be calculated from a system of Maxwell's equations. For an ensemble of metal and semiconductor NPs, eq 1 should be solved numerically. However, for a single, spherical NP this equation can be easily solved analytically (see the model in Fig. 1). In the steady-state regime, the local temperature around a single NP is described by a simple equation:

$$\Delta T(\mathbf{r}) = \frac{V_{NP} Q}{4\pi k_0 r^2} \quad (3)$$

where r is the distance from the center of an NP, k_0 is the thermal conductivity of the surrounding medium, and V_{NP} is the NP volume. Eq 3 is valid outside the NP, i.e. $r > R_{NP}$, where R_{NP} is the NP radius. The surrounding medium can be water, a chemical solution, or a polymer. We can also calculate analytically the heat generation Q , assuming that the wavelength of the incident light is much longer than the NP radius ($\lambda \gg R_{NP}$):

$$Q = \frac{\omega}{8\pi} E_0^2 \left| \frac{3\epsilon_0}{2\epsilon_0 + \epsilon_{NP}} \right|^2 \text{Im}\epsilon_{NP} \quad (4)$$

where E_0 is the amplitude of the incident radiation, and ϵ_{NP} and ϵ_0 are the dielectric constants of the NP and surrounding medium, respectively. The details of derivation can be found elsewhere³⁵.

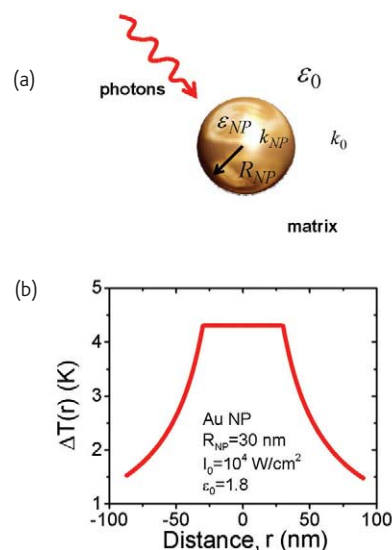


Fig. 1 (a) Schematic of an optically driven spherical nanoparticle. (b) Calculated temperature increase for a single Au NP as a function of the distance from the NP center. The surrounding medium is water.

The maximum temperature increase occurs at $r = R_{NP}$ and is given by:

$$\Delta T_{\max}(I_0) = \frac{R_{NP}^2 \omega}{3k_0 8\pi} \left| \frac{3\epsilon_0}{2\epsilon_0 + \epsilon_{NP}} \right|^2 \text{Im}\epsilon_{NP} \frac{8\pi \cdot I_0}{c\sqrt{\epsilon_0}} \quad (5)$$

where I_0 is the light intensity inside the matrix. This equation includes the important dependence of temperature on the NP size:

$$\Delta T_{\max} \propto R_{NP}^2 \quad (6)$$

The temperature increase is proportional to the second power of the NP radius. There are two factors leading to this dependence: (i) the total heat generation rate inside the NP is given by $V_{NP}Q$ and is proportional to the NP volume; and (ii) the total heat current from the NP surface is given by $k_0 S_{NP} \partial\Delta T/\partial r$, where S_{NP} is the NP surface area. Therefore, from the energy balance equation and an estimate $\partial\Delta T/\partial r \approx T/R_{NP}$, we obtain $\Delta T_{\max} \propto V_{NP}R_{NP} / S_{NP} \propto R_{NP}^2$. That is, the size dependence of the temperature increase is governed by the total rate of heat generation and by heat transfer through the NP surface.

The heat generation rate and temperature increase depend on the physical properties of a material. In particular, the imaginary part of the dielectric constant plays an important role (see eqs 3-5). Fig. 2 shows the total heat generation rate, $q_{\text{tot}} = V_{NP}Q$, for NPs composed of different materials. The dielectric constants were taken from tables elsewhere³⁶; for the matrix, we took water with a high-frequency dielectric constant. For metal NPs, the heat generation rate demonstrates a typical plasmon peak. It is interesting to note that a Ag NP under plasmon resonance conditions generates heat about ten times stronger than a Au NP. It is consistent with previous publications on plasmon resonances in Ag and Au, where Ag typically

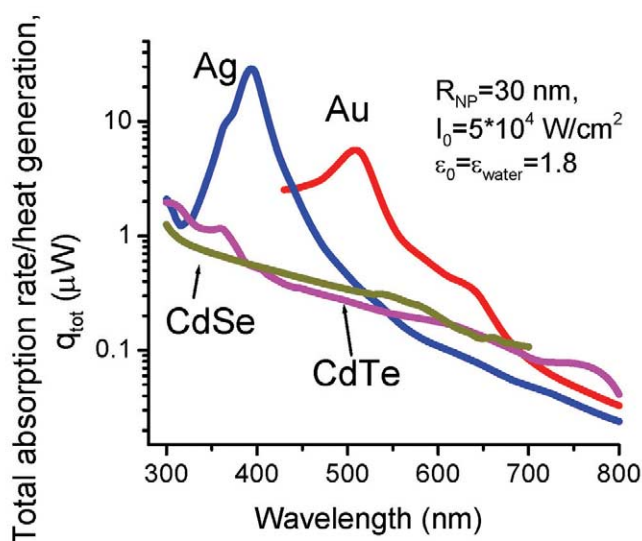


Fig. 2 Calculated rate of light energy dissipation in Au, Ag, CdTe⁴⁴, and CdSe⁴⁴ NPs.

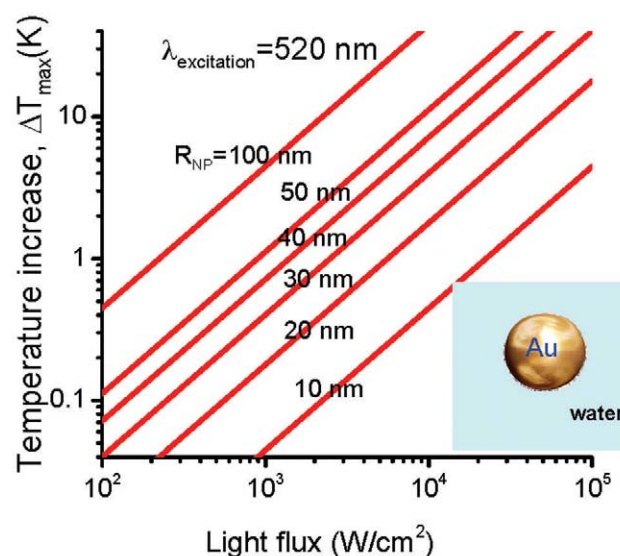


Fig. 3 Calculated temperature increase at the surface of a single Au NP in water as a function of illumination power at the plasmon resonance³⁵.

demonstrates much stronger plasmon enhancement^{37,38}. For typical semiconductors (CdTe, CdSe), the heat generation rate is much smaller. The corresponding heating mechanism in these materials is interband absorption. Note that our calculations were made with the bulk dielectric constant, therefore they do not include size-quantization effects. Strictly speaking, our estimates are valid for the blue part of the spectrum, $\lambda < \lambda_{\text{band edge}}$.

The data in Fig. 2 is given for a light flux of $I_0 = 5 \times 10^4 \text{ W/cm}^2$. If the laser spot diameter is about $2 \mu\text{m}$, the total light intensity becomes about $I_0A \approx 2 \text{ mW}$. In other words, a single Au NP (of 60 nm diameter) generates $5 \mu\text{W}$ of heat under illumination of 2 mW under the plasmon resonance condition ($\lambda \approx 520 \text{ nm}$). For a single Ag NP, the heat generation can be ten times larger. Of course, this small conversion rate ($2 \text{ mW} \rightarrow 5 \mu\text{W}$) comes from the fact that an NP has a much smaller diameter than the laser spot. If a system contains many NPs, the power conversion rate can be much larger.

Since Au NPs are the most common nanocrystals for nano- and bioapplications, we now calculate the temperature increase at the surface of Au NPs of different sizes. We can see from Fig. 3 that the temperature increase becomes noticeable (a few degrees) if the NP size is sufficiently large. Again, we note that for Ag NPs of a given size, the temperature increase can be ten times stronger.

Phase transformations

Heat generated by NPs by optical means can create a phase transformation in a surrounding matrix. Under steady-state conditions, such a process is described by eq 1 with the left-hand side equal to zero.

The simplest geometry can again be realized with a single spherical NP (see Fig. 4). The matrix material melts around a heat generator

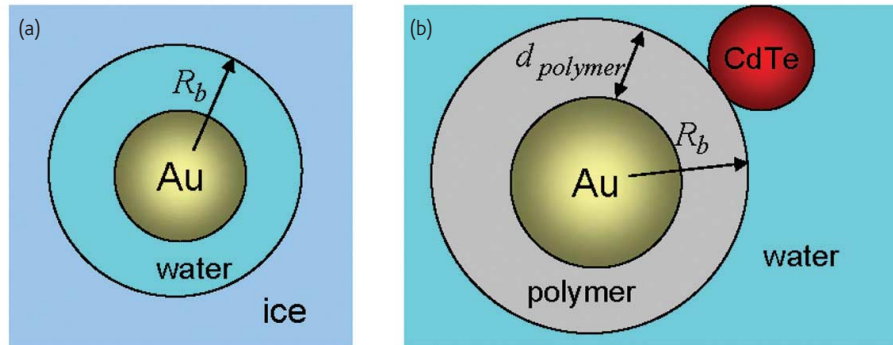


Fig. 4 (a) Schematic of metal NP embedded in ice. Heat released from the NP creates a spherical shell of liquid. (b) An optically driven NP can melt a polymer shell. The radius of the temperature-sensitive polymer R_b increases with light power. The CdTe NP serves to detect the process of polymer melting. (Reproduced with permission from³⁵. © 2006 Springer.)

(NP) and forms a spherical shell of liquid. The simplest material system in which to observe the melting effect is ice⁶. Fig. 5 shows the temperature distribution around an optically excited Au NP. To calculate this distribution, we used the thermal and dielectric parameters of ice and water. It is apparent from the inset of Fig. 5 that there is a critical light power at which the water shell forms. Experimentally, the process of melting can be recorded by looking at the Raman signal intensity of water/ice⁶. The critical power to melt the matrix around a spherical NP and the radius of the water/ice boundary are given by simple equations³⁵:

$$\frac{QR_{Au}^2}{3(T_{trans}-T_0)} > k_{solid}, R_b = \frac{QR_{Au}^3}{3k_{solid}(T_{trans}-T_0)} \quad (7)$$

where Q is given by eq 4, and T_{trans} and T_0 are the phase-transition temperature and equilibrium temperature of the matrix, respectively.

It has also been shown theoretically³⁵ that melting can be realized for a polymer shell (Fig. 4b). Again, this process starts if the

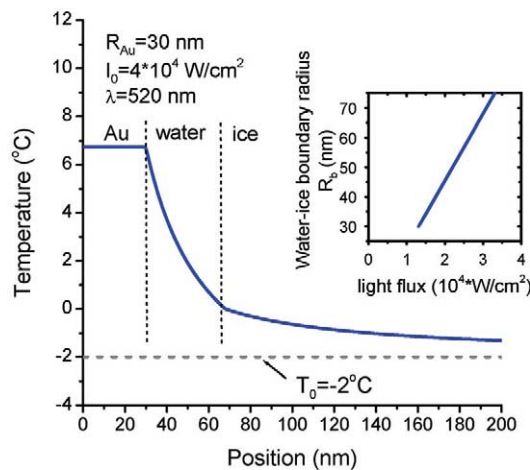


Fig. 5 Calculated temperature around an optically driven Au NP as a function of coordinate. Inset: Radius of water/ice interface as a function of light flux. The matrix is described with $\epsilon_{water} \approx \epsilon_{ice} = \epsilon_0 = 1.8$. (Reproduced with permission from³⁵. © 2006 Springer.)

illumination power is larger than a critical value. Similar structures have been assembled and studied optically²⁹. The authors used poly(ethylene glycol), or PEG, as the polymer²⁹. PEG undergoes a phase transition and increases its volume as the temperature changes from about 20°C to 40°C. Light-emitting CdTe NPs attached to a polymer shell (Fig. 4) served as a detector for the melting process. The emission intensity of CdTe NPs strongly depends on the distance from the Au NP. In this configuration, the Au NP causes an enhancement in the CdTe emission because of a resonant plasmon/exciton interaction. When the polymer melts, the CdTe-Au distance increases. Optically, this process can be seen as a decrease in CdTe-exciton emission.

Collective effects

The heating effect can be strongly enhanced in the presence of several NPs. Two mechanisms of interaction between NPs relate to the heating process: (i) accumulative effect; and (ii) Coulomb interaction.

The accumulative effect comes from the addition of heat fluxes generated by single NPs, and is described by the thermal diffusion equation (eq 1). The energy 'source' in this equation should be written as a sum over all NPs: $Q(r, t) = \sum_i Q_i(r, t)$, where $Q_i(r, t)$ describes heat generation by the i^{th} NP. The more NPs, the stronger the temperature increase that appears in the system (Fig. 6). This effect was clearly observed in the experimental study on melting of ice with Au NPs⁶.

The Coulomb interaction effect is more complicated. Since optically driven NPs interact through plasmon-enhanced electric fields (one NP 'feels' an electric field induced by others), the resultant heat depends on the inter-NP distance and NP arrangements. Fig. 7 shows our preliminary results for two NPs. We can see that the total amount of heat generated by two interacting NPs is different from the heat created by two single NPs. This is because of the partial screening of electric fields inside the NPs. The total heat dissipation can increase or decrease, depending on the incident light polarization. If the NP pairs are in solution and randomly oriented, the average heat generation can be enhanced or reduced. The effect may also come from the shift of plasmon resonance resulting from the inter-NP Coulomb interaction.

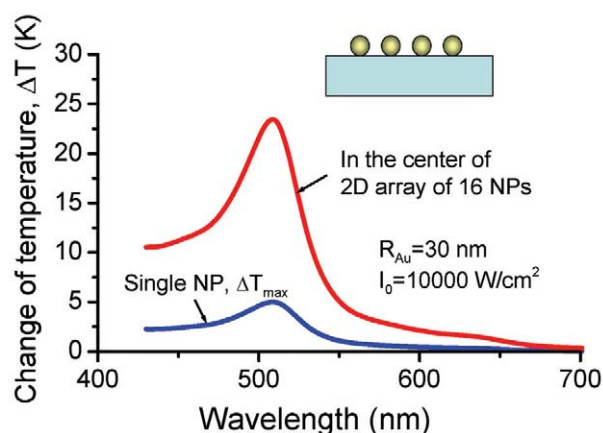


Fig. 6 Calculated temperature increase in the center of a square array of 16 NPs (4 × 4 array) at a polymer/water boundary. Inset: Model of an Au NP complex. $\epsilon_{\text{water}} \approx \epsilon_{\text{ice}} = \epsilon_0 = 1.8$. (Reprinted with permission from³⁵. © 2006 Springer.)

In this example, we took a relatively large inter-NP distance and the interaction effect turns out to be relatively small. We expect that for smaller inter-NP distances, the interaction will become much stronger. These results suggest that, for example, clustering of metal NPs can significantly affect the total heat generation.

Characterizing heat generated by optically driven Au NPs

Experimental procedure

The heat generated by optically driven Au NPs can be determined by placing the Au NPs in a matrix of known thermodynamic properties (in this case ice) and measuring the temperature change around the particles after optical excitation. Once the local temperature change

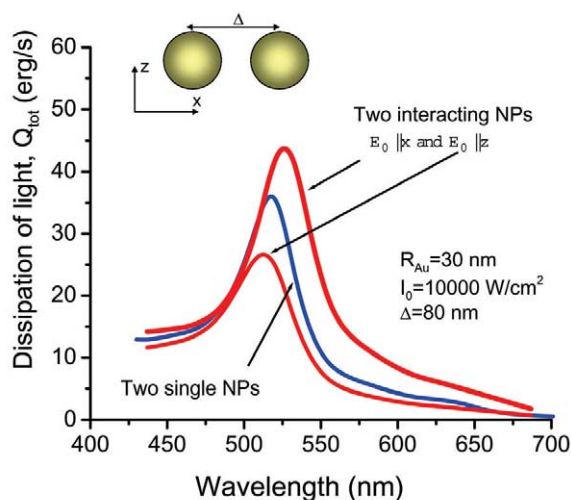


Fig. 7 Calculated rate of light energy dissipation in a system of two Au NPs for different polarizations of the incident photons. The dissipation rate of two NPs in the limit $\Delta \rightarrow \infty$ is also shown. Inset: Geometry of the system. (Reproduced with permission from³⁵. © 2006 Springer.)

is measured, then the amount of heat generated from the optically excited Au NP can be calculated from the simple theory developed above. The difficult part is measuring the local temperature change around the particles.

An experimental apparatus for measuring the temperature change around a Au NP or NP cluster during optical excitation is shown in Fig. 8. A sample cell is constructed from a Coverwell-Silicone Isolator chamber. A thermocouple (alumel/chromel 0.003” diameter purchased from Omega Engineering) is placed on top of a glass coverslip (300 μm thick) and a well is created for holding the Au NP solution (British Biocell International) by adhering the silicone isolator to the coverslip pinning the thermocouple inside the well. The Coverwell Silicone-Isolators (Electron Microscopy Sciences) are 3.0 mm in

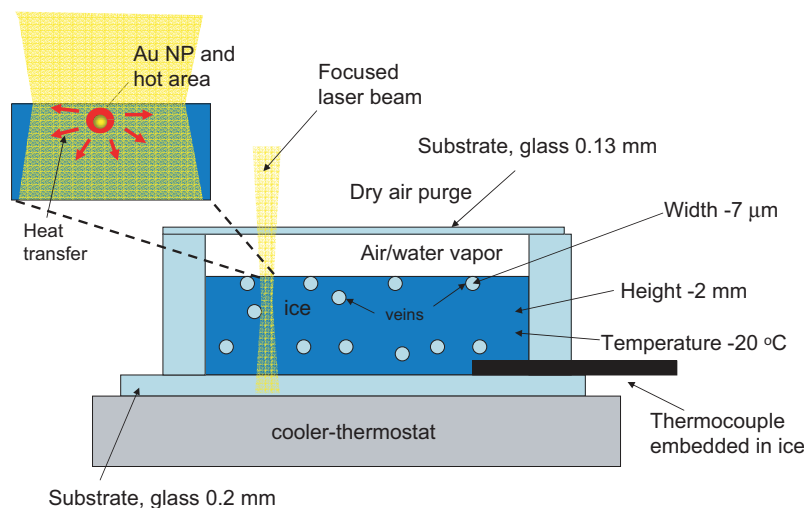


Fig. 8 Experimental setup with a well that contains ice with embedded Au NPs. Inset: 50 nm Au NP excited with focused laser beam and heat transfer to the ice matrix. (Reprinted with permission from⁶. © 2006 American Chemical Society.)

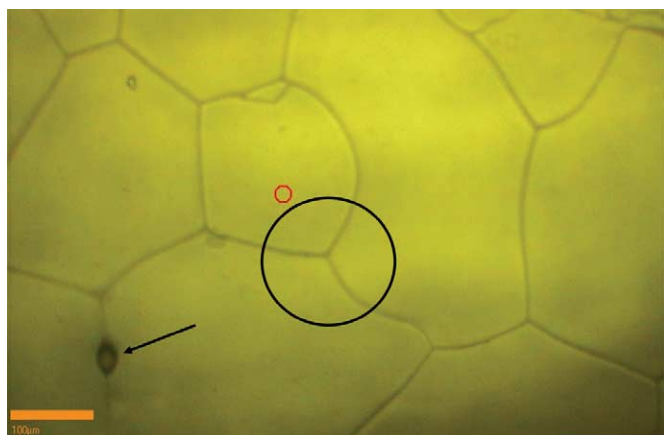


Fig. 9 Image of the ice surface showing grain boundaries. The circle in the middle of the image shows an intersection of three ice grains, while the arrow at the bottom of the image indicates a spot on a grain boundary that was irradiated with the laser. Scale bar = 100 μm .

diameter and 3.0 mm deep. A solution of 50 nm Au NPs is diluted with ultrapure 18 M Ω water to a concentration of 4.5×10^9 particles/cm³. Then 20.0 μL of solution is poured into the well and sealed with a thin (100 μm thick) coverslip. The sample apparatus is placed on a Peltier cooler housed inside a nitrogen-controlled climate box and the entire assembly is placed under a WiTec Raman/near-field scanning optical microscope. A 10x lens with a working distance of 7 mm was used to collect Raman and photoluminescence (PL) spectra using 532 nm laser excitation. The laser intensity was calibrated against the needle stop valve that restricts the opening aperture of the laser. The laser intensity was controlled from 0.2-50 mW using this needle stop. The laser spot size of the microscope operating in this configuration is 1.3 μm .

The liquid water was cooled until it froze. Typically, water solutions with Au NPs freeze at around -20°C . Many freeze/thaw cycles were necessary to degas the sample but, once this had been accomplished, large single crystals of ice ($\sim 200 \mu\text{m}$ on an edge) could be formed having extended vein structures³⁹. The sample was then cooled to -20.0°C and low laser intensity (0.5 mW) Raman images were collected to find the Au NPs.

Fig. 9 is an image of the surface of ice. The grain boundaries are clearly visible⁴⁰. The circle in the middle of the image highlights a typical intersection of grain boundaries. The blemish in the bottom of the image is a spot where melting was observed with laser excitation. Cratering of the ice is observed after extended laser irradiation.

Fig. 10 shows a Raman intensity map of a 100 $\mu\text{m} \times 100 \mu\text{m}$ section of the ice. The PL spectrum of the grain boundaries reveals a broad band centered on 560 nm (Fig. 10b). This band is assigned to plasmon emission of optically excited Au NPs. Similar optical emissions of Au NPs have been previously recorded^{41,42}. Typically, the Au NP plasmonic emission is weak. However, it has characteristic features (spectral position and shape) that allow us to detect it reliably. The largest emission from the Au NPs is observed at the grain boundaries, with a much smaller clustering of emission within the ice crystals.

The number of Au particles within the excitation area of 1.3 μm diameter was determined by comparing the PL integrated intensity from Au NPs in a liquid solution with known concentration to the integrated intensity of Au NPs in ice. An estimate for the number of NPs was obtained simply by dividing the PL signal of Au NPs in ice by the signal for a single Au NP in liquid solution within the excitation volume. This calibration could not be used to determine the structure

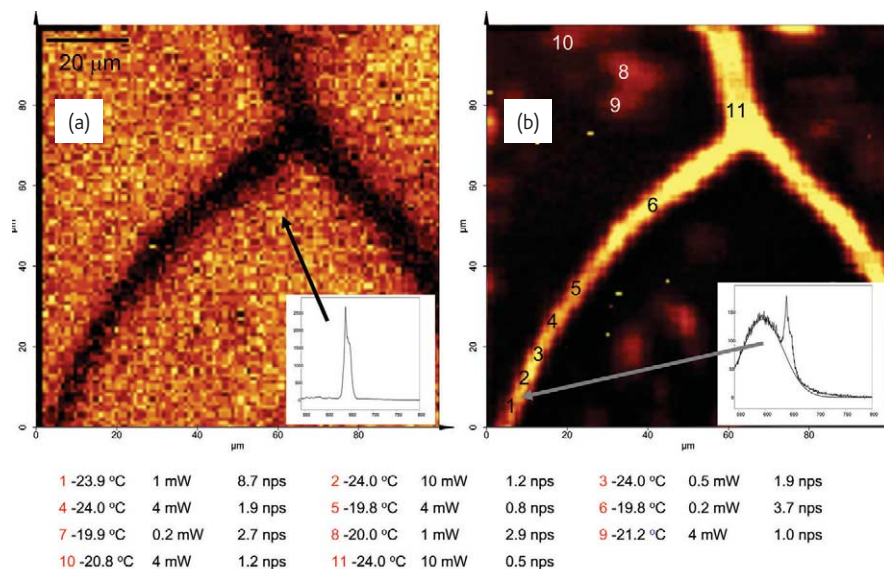


Fig. 10 (a) Raman intensity map of a 100 $\mu\text{m} \times 100 \mu\text{m}$ section of ice with 50 nm Au NPs embedded. Inset: Raman spectrum showing the ice peak. (b) PL intensity map of the same spatial area. 50 nm Au NPs are mostly trapped at the grain boundaries and exhibit a broad emission line around 600 nm. Inset: PL spectrum of 50 nm Au NPs. Bottom panel: Temperature, power, and estimated number of Au NPs within the laser spot for points labeled 1-11 in part (b). (Reprinted with permission from⁶. © 2006 American Chemical Society.)

or configuration of the Au NPs but only the number of particles within the excitation area.

Temperature change determination

Once the location and number of Au particles in the ice is determined, the threshold laser intensity that causes melting at a particular temperature is probed. The melting of ice in the absence of Au NPs was checked by irradiating grains of ice that did not contain any Au NPs. These regions do not melt even at the highest laser intensity of 50 mW. The sample was then moved to a previously determined spot containing a known number of particles. Time resolved Raman/emission spectra can be collected with a known laser intensity and sample temperature. This isothermal experiment was repeated, increasing the laser intensity, until the threshold laser intensity that caused melting was found. The threshold intensity was confirmed by observing a decrease in the time-resolved Raman intensity for ice.

Fig. 11 shows a typical family of time-resolved spectra collected at a particular spot. Melting of the ice can be confirmed visually as a crater observable with an optical microscope. This procedure allows us to map out the threshold laser intensity that causes melting as a function of temperature and particle number. Some of these spatial points along with the ice temperature, threshold laser intensity, and number of particles are shown in Fig. 10.

Time-resolved Raman spectra of ice collected with a laser intensity of 10 mW is shown in Fig. 12. The ice temperature is -20°C and the intensity is above the threshold for melting. Evidence of melting is apparent in the spectra in the loss of the ice peak intensity. The bottom of Fig. 12 shows the difference spectra using the initial ice spectrum as the reference spectrum. The difference spectra show only loss of ice with no conversion into liquid water. If water was formed, there would be a positive band in the difference spectrum where liquid

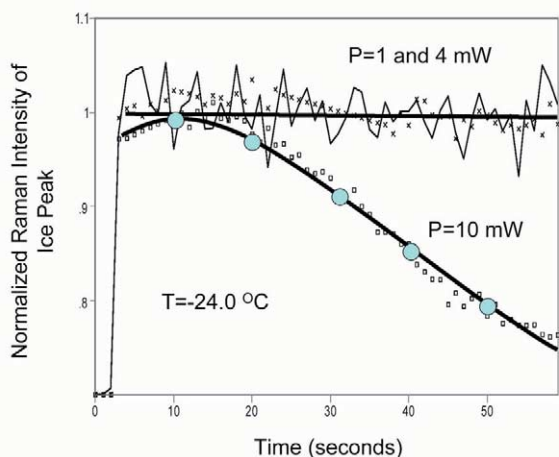


Fig. 11 Normalized Raman intensity for the ice peak as a function of time for three different laser beam intensities at position 2 in Fig. 10b. Solid lines are drawn for guidance. The temporal decrease of the Raman signal for $P = 10\text{ mW}$ indicates the melting process when $P > P_{\text{melting}}$. (Reprinted with permission from⁶. © 2006 American Chemical Society.)

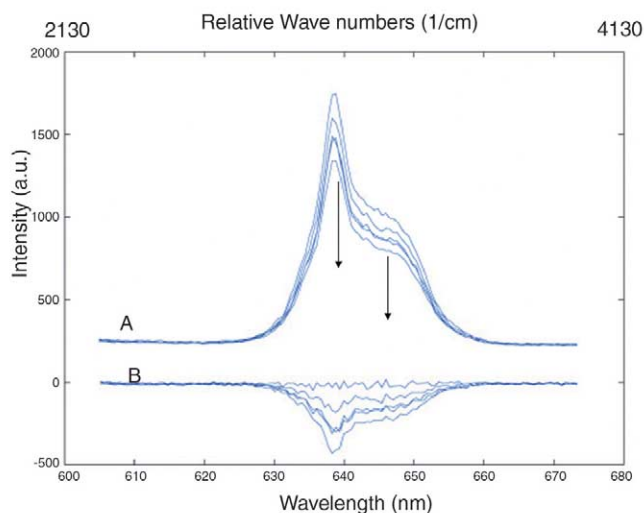


Fig. 12 (a) Time-resolved Raman spectra for ice during laser melting at the grain boundary. The ice peak decreases in intensity over time when the area is irradiated. (b) Difference Raman spectra showing the change in Raman intensity between the initial spectrum and spectra at later times. The difference spectra only show a negative peak from loss of ice. Conversion of ice into water would give a corresponding gain in intensity from water.

water absorbs. These results indicate that during laser excitation, the melted ice sublimates and a crater is created. This technique is extremely sensitive to the melting of ice because any melting results in loss of ice and subsequent loss in the Raman ice peak.

We should stress that the mapping of Au NPs and ice (Fig. 10) was performed noninvasively, i.e. at a very small intensity power that is not able to melt ice. Then, for several selected locations, we increased the laser power and observed the melting process as a temporal decrease in the Raman signal of ice. The above experiments were carried out for spots with relatively small numbers of Au NPs (< 10 ; see bottom panel in Fig. 10). Follow-up transmission electron microscopy analysis showed that there are also large agglomerates of Au NPs and such agglomerates can cause a very intensive melting process, which was observed.

Characterization of Au NP agglomerates

Au NPs are first immobilized on a surface by dipping a glass coverslip with a positively charged polymer⁴³ (poly(diallyldimethylammonium) or PDPA). The polymer-coated surface is rinsed with ultrapure $18\text{ M}\Omega$ water and dipped into a solution of negatively charged Au NPs. The Au NPs are held on the surface through electrostatic interactions. This surface is then rinsed with water and dried. The Au NPs immobilized on the surface can be characterized with respect to aggregation and heat generation by analyzing the plasmon emission from the Au particles.

Fig. 13 shows a $10\text{ }\mu\text{m} \times 10\text{ }\mu\text{m}$ image of a coverslip with Au NPs immobilized on it. The plasmon emission from one of the Au agglomerates is shown in the inset. The peak intensity is around 560 nm . The integrated intensity from 550 nm to 700 nm of the PL spectrum for each pixel in the image is plotted. The excitation laser

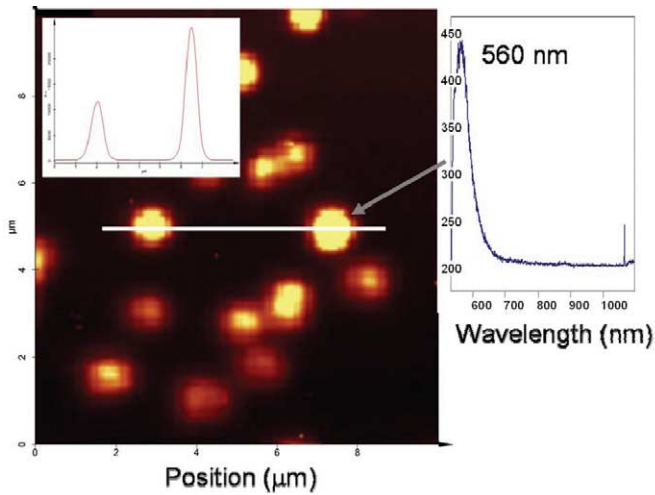


Fig. 13 Image showing PL integrated intensity of Au NPs immobilized on a glass coverslip. The plasmon emission from one of the Au agglomerates is shown in the right-hand inset. The excitation laser wavelength is 532 nm and the peak intensity is 560 nm. A cross section through two agglomerates (shown as the line in the image) is plotted in the left-hand inset. The peak height of the second agglomerate is roughly twice that of the first agglomerate.

wavelength is 532 nm. The cross section through two agglomerates (shown as the line in the image and plotted in the upper inset) reveals that the intensity from the second agglomerate is roughly twice that of the first agglomerate. The maximum peak intensity for each cluster is determined and a histogram (shown in Fig. 14) is constructed. The top histogram (Fig. 14a) is constructed from the peak maximum along the spatial contour using the integrated intensities from the plasmon emission. These peak intensities are divided by the lowest peak intensity to obtain a normalized histogram shown in Fig. 14b. Integer

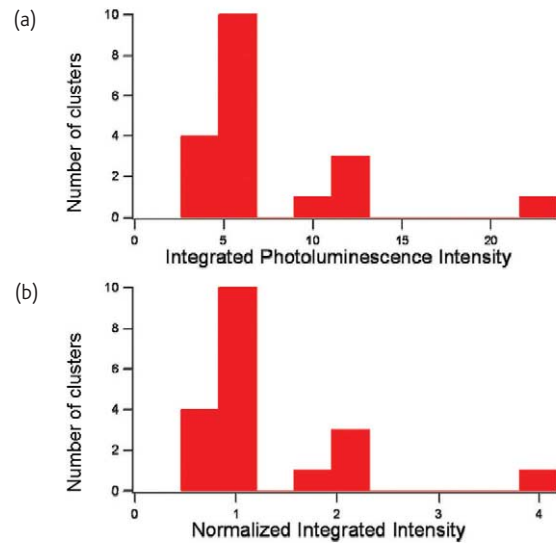


Fig. 14 (a) Histogram constructed from the peak maximum of pixels in the image using the PL integrated intensity. (b) Histogram of the normalized PL integrated intensity showing integer spacing of the histogram peaks. The normalized integrated intensity is obtained by dividing all of the intensities in part (a) by the lowest intensity.

spacing between the histogram peaks confirms that the plasmon emission scales with the number of Au NPs in the agglomerate. The number of Au NPs in any cluster, aggregate, or agglomerate can be determined by measuring the plasmon emission from a distribution of different Au NP clusters.

Comparison between theory and experiment

Fig. 15a shows measured melting power versus background temperature for different positions on the ice surface (Fig. 10).

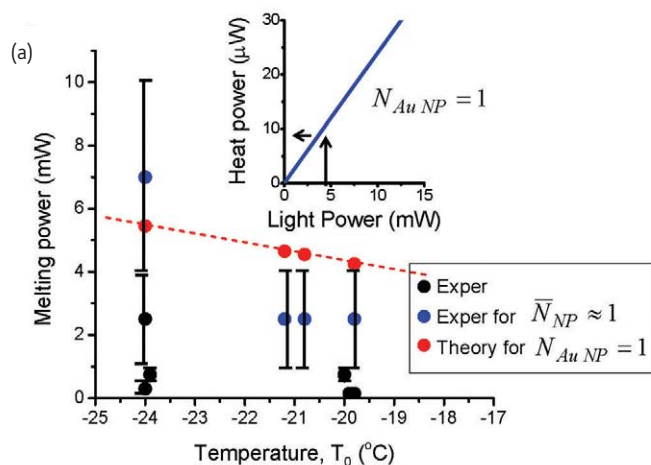
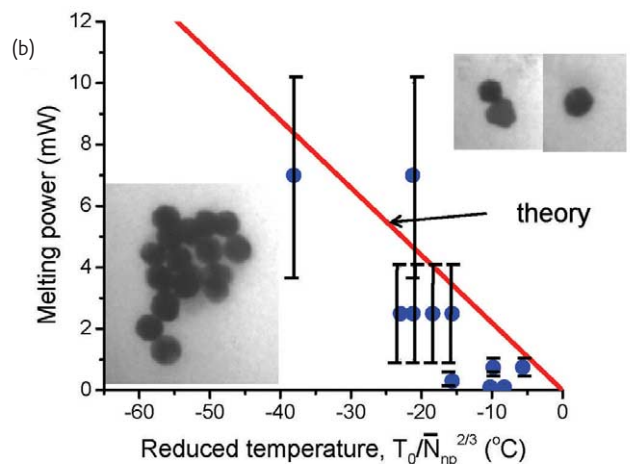


Fig. 15 (a) Black and blue dots represent experimental data for the melting power from positions 1–11 in Fig. 10b as a function of the thermostat temperature. The blue dots correspond to the four positions with an estimated number of Au NPs $N_{AuNP} \approx 1$. Red dots are the calculated data for a single Au NP of 50 nm diameter. Inset: calculated heat power released by a single 50 nm Au NP as a function of the laser power. Arrows show the case for $P_{melting} = 4$ mW. (b) Dots represent experimental data for the melting power as a function of the reduced temperature T_{red} . The red curve comes from the simple model described. Insets: transmission electron micrographs of several 50 nm Au NP complexes found in the solution after melting the ice. (Reprinted with permission from⁶. © 2006 American Chemical Society.)



Theoretically, the melting power is given by the condition $T_{\max} = T_{\text{trans}}$ that leads to $Q = k_{\text{ice}} 3(T_{\text{trans}} - T_0) / R_{\text{Au}}^2$. Since $P_{\text{melting}} \sim Q$:

$$P_{\text{melting}} \sim (T_{\text{trans}} - T_0) / R_{\text{Au}}^2 = -T_0 / R_{\text{Au}}^2 \quad (8)$$

with $T_{\text{trans}} = 0^\circ\text{C}$ for the ice/water system. We also show as red dots calculated melting power for a complex of one NP.

To compare experiment and theory properly, we should take into account the fact that we measure Au NP complexes. For this, we introduce a reduced temperature $T_{\text{red}} = T_0 / N_{\text{AuNP}}^{2/3}$, where N_{AuNP} is the number of NPs, and so $P_{\text{melting}} \propto T_{\text{red}} = T_0 / N_{\text{AuNP}}^{2/3}$. The reduced temperature parameter reflects the fact that, if the number N_{AuNP} is small, the magnitude of the reduced temperature is larger, and we need to use a more powerful laser beam to melt the matrix. To derive the scaling factor $1/N_{\text{AuNP}}^{2/3}$, we now assume that a complex of N_{AuNP} NPs acts as a single nanosphere of volume $V_{\text{tot}} = (4\pi/3) R_{\text{NP}}^3 N_{\text{AuNP}}$. Then, the resulting radius of the nanosphere is $R_{\text{tot}} = R_{\text{NP}} N_{\text{AuNP}}^{1/3}$. Using eq 8, we obtain the melting power for the nanosphere:

$P_{\text{melting}} \sim -T_0 / R_{\text{tot}}^2 \sim -T_0 / N_{\text{AuNP}}^{2/3}$. In other words, the melting power for NP complexes is proportional to the reduced temperature T_{red} . Of course, this derivation ignores some of the features of the

physical picture, such as the granular structure of the complex and inter-NP interactions. More details of this derivation can be found elsewhere^{6,35}. Fig. 15b shows melting powers versus reduced temperature, as well as theoretical results. We find overall good agreement between theory and experiment. The results indicate that the thermal interactions between NPs are very important, and the actual temperature on the surface of the NP complex depends on the NP number and arrangement^{6,35}.

Summary

Photothermal effects at the nanoscale represent an interesting problem that may have important applications. The most challenging problems are in the measurement of local temperature at the surface of NPs and heat transfer through molecular linkers. Insights into these problems can be made through phase transformations of the surrounding matrix. In NP assemblies, interaction between NPs strongly changes thermal properties such as heat generation and local temperature. ■

Acknowledgments

This work was supported by the BioNanoTechnology Initiative at Ohio University. The authors thank Alyssa Thomas for help with the manuscript preparation.

REFERENCES

- Murray, C. B., et al., *J. Am. Chem. Soc.* (1993) **115**, 8706
- Yu, S. H., et al., *Langmuir* (2001) **17**, 1700
- Jiang, J., et al., *J. Phys. Chem. B* (2003) **107**, 9964
- Sawitowski, T., et al., *Adv. Func. Mater.* (2001) **11**, 435
- Fukushima, M., et al., *Thin Solid Films* (2003) **438**, 39
- Richardson, H. H., et al., *Nano Lett.* (2006) **6**, 783
- Elghanian, R., et al., *Science* (1997) **277**, 1078
- Compton, D., et al., *Gold Bull.* (2003) **36**, 51
- Schrof, W., et al., *Adv. Mater.* (1998) **10**, 338
- Aweeka, T., *MRS Bull.* (2006) **31**, 653
- Tan, Y., et al., *J. Nanosci. Nanotechnol.* (2006) **6**, 262
- Eustis, S., and El-Sayed, M. A., *Chem. Soc. Rev.* (2006) **35**, 209
- Teranishi, T., et al., *Adv. Mater.* (2001) **13**, 1699
- Pissuwan, D., et al., *Trends Biotechnol.* (2006) **24**, 62
- Akamatsu, K., and Deki, S., *J. Colloids Interface Sci.* (1999) **214**, 353
- Akamatsu, K., and Deki, S., *J. Mater. Chem.* (1998) **8**, 637
- Shimizu, T., et al., *J. Phys. Chem. B* (2003) **107**, 2719
- El Roustom, B., et al., *Electrochem. Commun.* (2005) **7**, 398
- Tsai, C. Y., et al., *Mater. Lett.* (2004) **58**, 1461
- Sun, X. P., et al., *Macromol. Rapid Commun.* (2003) **24**, 1024
- Plech, A., et al., *Phys. Rev. B* (2004) **70**, 195423
- Armendariz, V., et al., *Rev. Mex. Fis.* (2004) **50**, 7
- Hu, M., et al., *Chem. Phys. Lett.* (2003) **372**, 767
- Maye, M. M., et al., *Langmuir* (2000) **16**, 490
- Huang, X. H., et al., *J. Am. Chem. Soc.* (2006) **128**, 2115
- Gobin, A. M., et al., *Lasers Surg. Med.* (2005) **37**, 123
- Leary, S. P., et al., *Neurosurgery* (2006) **58**, 1009
- Jain, P. K., et al., *J. Phys. Chem. B* (2006) **110**, 7238
- Lee, J., et al., *Angew. Chem. Int. Ed.* (2005) **44**, 7439
- Xia, Y. N., and Halas, N. J., *MRS Bull.* (2005) **30**, 338
- Boyer, D., et al., *Science* (2002) **297**, 1160
- Skirtach, A. G., et al., *Nano Lett.* (2005) **5**, 1371
- Skirtach, A. G., et al., *Angew. Chem. Int. Ed.* (2006) **45**, 4612
- Liu, G. L., et al., *Nat. Mater.* (2006) **5**, 27
- Govorov, A. O., et al., *Nanoscale Res. Lett.* (2006) **1**, 84
- Palik, E. D., *Handbook of Optical Constants of Solids*, Academic Press, New York, (1985)
- Lee, J., et al., *Nano Lett.* (2004) **4**, 2323
- Lee, K. S., and El-Sayed, M. A., *J. Phys. Chem. B* (2006) **110**, 19220
- Richardson, H. H. J., *Molec. Struct.* (2006), in press
- Nye, J. F., *J. Glac.* (1989) **35**, 17
- Dulkeith, E., et al., *Phys. Rev. B* (2004) **70**, 205424
- Varnavski, O. P., et al., *J. Phys. Chem. B* (2003) **107**, 3101
- Zhang, H., et al., *J. Phys. Chem. B* (2006) **110**, 2171
- Hernandez, P., et al., unpublished results